Towards Droplet Dynamics Simulation in Polymer Electrolyte Membrane Fuel Cells: Three–Dimensional Numerical Modeling of Confined Water Droplets with Dynamic Contact Angle and Hysteresis

Mohammad R. Hashemi,[1,2] Pavel B. Ryzhakov,[1,2] and Riccardo Rossi[1,2]

[1)]*Centre Internacional de Mètodes Numèrics en Enginyeria (CIMNE), 08034 Barcelona, Spain.*

[2)]*Universitat Politècnica de Catalunya (UPC), 08034 Barcelona, Spain.*

(*Electronic mail: mhashemi@cimne.upc.edu)

(Dated: 20 November 2021)

This work focuses on three-dimensional simulation of the dynamics of droplets with contact–angle hysteresis. In order to consistently model the dynamics of the contact–line, a combination of the linear molecular kinetic theory and the hydrodynamic theory is implemented in the present numerical method. Without presetting the contact–line and/or the contact–angle, such simulations are generally prone to irregularities at the contact–line, which are mainly due to the imposition of the pinning and unpinning mechanisms associated with the hysteresis phenomenon. An effective treatment for this issue is proposed based on a simple procedure for calculating the nodal contact–angle within the framework of enriched finite element/level set method. The resulting method also benefits from a manipulated momentum conservation equation that incorporates the effect of the liquid mass conservation correction, which is essentially important for simulations with a rather long (physical) run–time. In this paper, the proposed numerical model is validated against the previously published experimental data addressing the configuration of a water droplet on a tilted rough hydrophobic surface. In this test, the effect of the the contact–line pinning as the underlying mechanism for droplet hysteresis phenomenon is also studied. The model is further employed to simulate a liquid droplet confined in a channel in the presence of air flow.

I. INTRODUCTION

Polymer electrolyte membrane (PEM) fuel cells (also known as proton exchange membrane fuel cells) are powerful modern energy conversion devices, known for their high efficiency and ambient-friendliness[1]. Despite the promising potential of PEM fuel cells to become one of the main sources of clean energy for transportation purposes[2], their usage is still hindered by their durability[3]. Water management[4] is among the challenging issues that directly affect the performance and durability of PEM fuel cells[5]. Efficient water management requires the evacuation of the water droplets that breakthrough the outer face of the gas diffusion layer (GDL) into the gas channel (GC). This evacuation is mediated by the air flowing in the GC at the cathode. Particular attention is paid to the prediction of the droplet detachment conditions, which, in turn, lead to insights regarding the efficiency of water evacuation for a given operation regime.

In this context, the analysis of the dynamics of water droplets confined in the GC is of main importance[6], which requires the incorporation of the complex wettability characteristics of the outer face of the GDL[7,8]. In such analyses, besides the experimental investigations and deliberate measurements and/or visualizations, numerical modelling can be acquired as a viable means to provide fundamental understanding of the phenomena.

For the numerical analysis of droplet dynamics in GC, one of the major requirements is to incorporate a dynamic (non–static) contact–angle[9,10] along with the prerequisites of the hysteresis phenomenon[11]. The latter is of particular importance due to the physicochemical properties of the fibrous substrate formed by the face of GDL[12]. Once the equilibrium condition at the three-phase contact–line is disturbed, unbalanced interfacial forces provide a tendency towards a new equilibrium leading to either wetting or dewetting process. The dynamic behavior the contact–angle[13] during these complex processes cannot be characterized by the Young's relation [14,15] anymore, as the mentioned law is limited to the definition of the static equilibrium contact–angle. It should be noted that modeling of the droplet dynamics on solid substrates has a vast range of applications from spray cooling[16,17] to fundamental biological phenomena[18].

The main approaches for the modeling of the contact–line dynamics are the molecular–kinetic[19,20] and hydrodynamic[21,22] theories with former focusing on the dissipation at the inter–molecular length–scale and latter treating the movement of the contact–line at the continuum–level. Nevertheless, recent studies[23,24] have revealed that the improved results are obtained when using a combination[25] of these two approaches.

One of the major complexities in the droplet spreading modeling is the contact–angle hysteresis phenomenon[26,27]. Hysteresis is associated with the pinning of the contact–line[28] and characterized by receding and advancing contact–angles[29], which are linked to the dewetting and wetting processes, respectively. This phenomenon is basically caused by the chemical properties[30], or more accurately by the heterogeneity[31,32] in the properties of the solid substrate that comes into contact with the gas and liquid phases. Surface roughness and its micro–structure are also among determining factors that cause dramatic variations in the contact–angle hysteresis[33–35].

Recent advances in the numerical modeling of multi–phase flows allowed to establish a reliable basis for the numerical simulation of the transport of water droplets in GC[10,11,36,37]. The numerical approaches in this context can be classified within the main categories of the phase–field models and the sharp–interface capturing techniques. The framework of the phase–field models provides a means to capture the dynamics of the contact–line without prior imposition of any specific dynamic contact–angle model[38]. Nevertheless, the phase–field models require an extreme mesh refinement in the vicinity of the liquid-gas interface, which leads to prohibitively high computational costs in three–dimensional simulations. The most used interface–capturing techniques on the other hand are the volume of fluid (VOF)[39] and the level–set method[40]. While the VOF method perfectly preserves the mass conservation, it lacks a systematic and efficient mechanism for reproduction of the geometric data associated with the liquid–gas interface. Unlike VOF, the level–set method circumvents the complexities associated with the calculation of the necessary geometric data, though it needs additional treatment for mass conservation preservation[41–43]. Besides these Eulerian approaches, a Lagrangian framework can also be acquired in this field[44,45]. However, the employment of such a Lagrangian approach in three-dimensional cases would lead to a prohibitively high computational cost.

Authors have recently introduced enriched finite element / level–set method[46,47] that creates a framework for a sharp (zero–thickness) interface treatment, which is a key for efficient simulation of droplet dynamics. Moreover, this method allows for the direct implementation of experimentally admitted dynamic contact–line models. In the present work, the method is further developed by incorporating a consistent treatment of the contact–angle hysteresis phenomenon. The current numerical method models the dynamic contact–angle by a combination of the molecular–kinetic and the hydrodynamic theories. Additionally, in this paper, a simple mass conservation improvement technique is introduced and the effect of the corresponding correction term on the momentum conservation equation is incorporated.

In the following, first, the governing equations and the hysteresis modeling technique are briefly discussed. The level–set method, the corresponding contact–angle calculation, and the (liquid) mass conservation treatment technique are described afterwards. Next, the incorporation of the mass conservation correction into the momentum conservation equation, and consequently, the variational formulation are derived. At the end of section II, a summary of the proposed numerical algorithm is provided. In section III, first, the impact of incorporating the mass conservation correction term into the momentum equation is shown. Afterwards, the proposed method is validated and applied to the tests involving the dynamics of a water droplet on the outer surface of a GDL with an emphasis on the hysteresis phenomenon. The essential importance of imposing a pinning mechanism for obtaining realistic results is analyzed in these tests.

II. NUMERICAL METHOD

A. Governing Equations

The gas-liquid system under consideration involves air and water. The flow of each homogeneous phase Ω_i, $i \in l, g$ of this system can be described by momentum

$$\rho\left(\frac{\partial \mathbf{u}}{\partial t} + \mathbf{u}\cdot\nabla\mathbf{u}\right) = \rho\mathbf{b} - \nabla p + \mu\nabla^2\mathbf{u} \quad \text{in}\,\Omega_i, \tag{1}$$

and mass

$$\nabla\cdot\mathbf{u} = 0 \quad \text{in}\,\Omega_i, \tag{2}$$

conservation equations, which are derived for incompressible Newtonian fluids. In the above equations, $\mathbf{u}$ is velocity, p is pressure, and $\mathbf{b} = -g\mathbf{e}_z$ denotes the body force, with ρ and μ being density and dynamic viscosity of the fluid phase, respectively.

Governing equations (1-2) are subject to the initial as well as the Dirichlet and Neumann boundary conditions, which read

$$\mathbf{u}(\mathbf{x},0) = \mathbf{u}_0 \quad \text{in}\,\Omega, \tag{3}$$

$$\mathbf{u}(\mathbf{x},t) = \mathbf{u}_D \quad \text{on}\,\partial\Omega_D, \tag{4}$$

and

$$\mathbf{T}(\mathbf{x},t) = \mathbf{T}_N \quad \text{on}\,\partial\Omega_N, \tag{5}$$

respectively, where $\mathbf{T}$ denotes the traction vector.

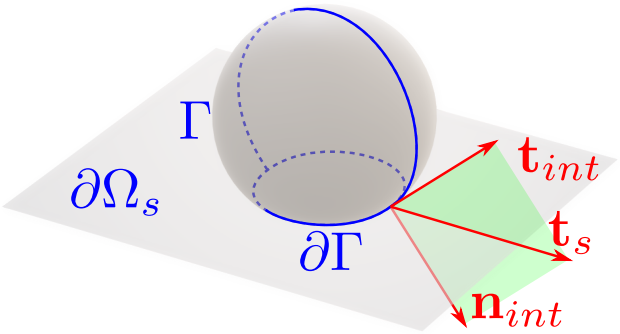

FIG. 1. Schematic of a droplet lying on a solid substrate. Unit vectors $\mathbf{t}_{int}$, $\mathbf{t}_s$, and $\mathbf{n}_{int}$ are all in the same plane, which is perpendicular to $\partial\Omega_s$. Contact–angle is the supplementary of the angle between unit vectors $\mathbf{t}_{int}$ and $\mathbf{t}_s$.

The liquid–gas interface (see Fig. 1), $\Gamma = (\Omega_l \cap \Omega_g)$, partially determines the boundary of each homogeneous phase and is subject to the following conditions

$$[\![\mathbf{T}(\mathbf{x},t)]\!] = -\gamma\kappa\mathbf{n}_{int} \quad \text{on}\,\Gamma, \tag{6}$$

and

$$[\![\mathbf{u}(\mathbf{x},t)]\!] = 0 \quad \text{on}\,\Gamma, \tag{7}$$

where γ and κ are the surface tension coefficient and the local curvature of the interface, respectively. In these equations, $\mathbf{T}$ represents the traction vector, $\mathbf{n}$ is the outward normal vector, and $[\![\cdot]\!]$ denotes the jump operator with respect to $\partial\Omega$. For a Newtonian fluid, the traction vector is calculated as

$$\mathbf{T} = \left[-p\mathbb{I} + \mu\left(\nabla\mathbf{u} + \nabla\mathbf{u}^T\right)\right]\cdot\mathbf{n}. \tag{8}$$

In case the interface is located at the solid substrate (see Fig. 1), the equilibrium condition[48] dictates that the liquid–gas surface tension must be balanced by liquid–solid (γ_{ls}) and gas–solid (γ_{gs}) interfacial tensions at the contact–line, $\partial\Gamma = (\partial\Omega_s \cap \Gamma)$. This gives the Young's relation[14,49]

$$\gamma\cos(\theta_Y) + \gamma_{ls} = \gamma_{gs}. \tag{9}$$

with θ_Y denoting the equilibrium contact angle. Once the equilibrium is disturbed, a model for incorporating the unbalanced interfacial forces (that are rendered to the Young stress) is required[50],

$$\tau_Y = \gamma[\cos(\theta_Y) - \cos(\theta)], \tag{10}$$

which is a function of the dynamic contact–angle, θ. In this work, the (simplified) linear molecular kinetic theory[13]

$$\tau_Y = \zeta u_{slip} \quad \text{on}\, \partial\Gamma, \tag{11}$$

with constant coefficient of friction ζ is used to model the dynamics of the contact–line. Here, $u_{slip} = \mathbf{t}_s \cdot \mathbf{u}$ is the local slip velocity of the contact–line. Taking into account nanometric (physical) length–scale and l_{micro} associated with the dynamic contact–angle, one can use the hydrodynamic theory[21], to correlate numerically captured contact–angle θ^{num} to microscopic θ as

$$\theta^3 = (\theta^{num})^3 - 9\frac{\mu u_{slip}}{\gamma}\ln(\frac{h_e}{l_{micro}}), \tag{12}$$

where h_e denote the length–scale associated with the resolution of the computational mesh (see[47] for more details). It must be noted that fixing parameters ζ and l_{micro} needs deliberately designed experiments[13].

Another complexity associated with the modeling of the moving contact–line is the stress singularity occurring in the vicinity of the contact–line if one tries to treat the solid substrate as a no–slip boundary[51]. The good practice to resolve this issue is to substitute the no–slip condition on the solid substrate with the Navier–slip condition formulated as[52]

$$\mathbf{n}_s \cdot \mathbf{u} = 0 \quad \text{on}\, \partial\Omega_s, \tag{13}$$

and

$$(\mathbb{I} - \mathbf{n}_s \otimes \mathbf{n}_s) \cdot \mathbf{T} = -\beta \mathbf{u} \quad \text{on}\, \partial\Omega_s, \tag{14}$$

with $\mathbb{I}$ and $\mathbf{n}_s$ being the identity tensor and the vector normal to the solid substrate, respectively.

B. Hysteresis

In the numerical modeling, the hysteresis phenomenon is generally rendered into the contact–line pinning conditions:

$$\text{contact–line is} \begin{cases} \text{free for wetting} & \text{if}\, \theta \geq \theta_A \\ \text{pinned} & \text{if}\, \theta_R < \theta < \theta_A \\ \text{free for dewetting} & \text{if}\, \theta \leq \theta_R \end{cases} \tag{15}$$

Here, θ_A and θ_R are the static advancing and the static receding contact–angles that characterize the pinning threshold[53]. Therefore, the (static) contact–angle hysteresis is calculated as $\Delta\theta_{static} =$

$\theta_A - \theta_R$[29]. In order to prevent confusion, it should be noted that in this work, θ_a and θ_r (with lower–case subscripts) denote the maximum and the minimum contact–angles, respectively. In this way, the instantaneous contact–angle hysteresis can be measured as $\Delta\theta = \theta_a - \theta_r$.

Besides implementing the pinning condition (15), in order to make the whole formulation consistent with the physical interpretation of hysteresis phenomenon[40], the equilibrium contact–angle, θ_Y, that appears in the definition of the unbalanced Young stress (10) is also set according to

$$\theta_Y = \begin{cases} \theta_A & \text{if wetting} \\ \theta & \text{if pinned} \\ \theta_R & \text{if dewetting} \end{cases} \tag{16}$$

This guarantees that while pinned, the contact–line has no tendency for movement. It is necessary to highlight that checking the liquid spreading direction, *i.e.* being in the wetting or dewetting regime, is of high importance for the physically justified incorporation of the pinning mechanism via conditions (15) and (16).

C. Level–set Method

The level–set method[54] is a robust interface capturing approach based on the convection of the continuous signed distance function, ϕ, according to

$$\frac{\partial \phi}{\partial t} + \mathbf{u} \cdot \nabla \phi = 0 \quad \text{in}\, \Omega. \tag{17}$$

The theoretical definition of ϕ reads

$$\phi(\mathbf{x},t) = \begin{cases} -d & \text{if}\, \mathbf{x} \in \Omega_l \\ 0 & \text{if}\, \mathbf{x} \in \Gamma \\ d & \text{if}\, \mathbf{x} \in \Omega_g \end{cases} \tag{18}$$

with d being the distance $\mathbf{x}$ from the interface, or equivalently, $\|\nabla\phi\| = 1$. Using level–set function ϕ, the wetting and dewetting can easily be formulated in the vicinity of the contact–line as

$$\frac{\partial \phi(\mathbf{x},t)}{\partial t} = \begin{cases} < 0 & \text{if wetting} \\ > 0 & \text{if dewetting} \end{cases} \tag{19}$$

During the evolution of the interface, there is a high chance of the occurrence of irregularities in level–set function ϕ that are re-presentable as a deviation from the true distance function (i.e.

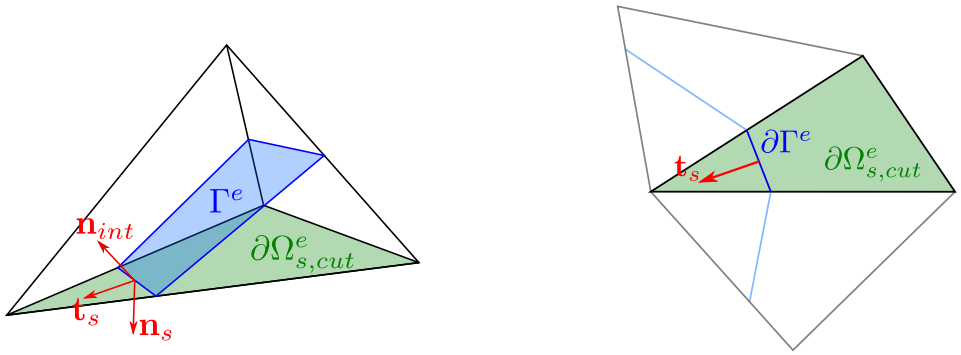

(a) (b)

FIG. 2. Schematics of (a) A cut element, Ω^e_{cut}, and (b) the corresponding contact–line, $\partial\Gamma^e$.

$\|\nabla\phi\| \neq 1$) and/or noise in the reproduced interface[46]. In order to address these irregularities, distance re-initialization[55] and level–set smoothing[47] techniques are utilized in the present method. The descretization of Eq. (17) is done using the streamline–upwind Petrov–Galerkin (SUPG) approach with the addition of the cross–wind stabilization term[56].

1. Contact–angle Calculation

Figure 2 illustrates a cut element located on the solid substrate and the associated unit vectors, $\mathbf{n}_{int}$, $\mathbf{n}_s$, and $\mathbf{t}_s$. Based on the definition of the level–set function, the normal vector to the interface can be calculated as

$$\mathbf{n}_{int} = \frac{\nabla\phi}{\|\nabla\phi\|}$$

In this way, the numerical contact–angle corresponding to the cut element is obtained as

$$\theta_e^{num} = \pi - \cos^{-1}\left(\mathbf{n}_s \cdot \frac{\nabla\phi}{\|\nabla\phi\|}\right). \tag{20}$$

The tangent to the substrate (normal to the contact–line) is also simply calculable as

$$\mathbf{t}_s = \frac{1}{\sin(\theta_e^{num})}\left[\mathbf{n}_s \times (\mathbf{n}_s \times \mathbf{n}_{int})\right].$$

In order to prevent inadequate imposition of the pinning condition, it is necessary to obtain regularly distributed contact–angle values. In the present work, the pinning condition (15) is selected based on the nodal value of the contact–angle, calculated as

$$\theta_I^{num} = \frac{1}{\left|\mathscr{E}_I^{cl}\right|}\sum_{e\in\mathscr{E}_I^{cl}} \theta_e^{num}, \tag{21}$$

where $\left|\mathscr{E}_I^{cl}\right|$ denotes the size of $\mathscr{E}_I^{cl}$, which is the set of elements that are cut by the contact–line and share node I. As long as a node is pinned according to condition (15), the corresponding value of level–set function ϕ is fixed and treated as a known value during the assembly of the system of equations obtained by discretization of Eq. (17).

2. *Mass Conservation Correction*

As shown in the literature[57], the level–set method does not guarantee the conservation of the mass of the fluid phases. Although (adaptive) mesh refinement[58] and higher–order methods[42] can be utilized to prevent any mass loss, a simple and efficient approach to compensate for this adverse artifact is a global correction to the level-set field. This can be defined as

$$\phi_{corr} = \phi + \frac{\int_{\Omega,liq} d\Omega - \mathscr{V}_{liq,0}}{\int_\Gamma d\Gamma}, \tag{22}$$

where ϕ_{corr} denotes the corrected level-set field and $V_{liq,0}$ is the initial volume of the liquid phase including the net liquid inflow. The volume correction term can equivalently be represented in term of pseudo-velocity

$$u'_{int} = -\frac{1}{dt}\frac{\int_{\Omega,liq} d\Omega - \mathscr{V}_{liq,0}}{\int_\Gamma d\Gamma}. \tag{23}$$

Nonetheless, employing a volume correction technique requires correcting the momentum conservation equation accordingly. Without loss of generality, consider a case with volume loss; the pseudo–velocity is positive and consequently, the mass correction procedure increases the momentum of the liquid phase while the gas momentum is decreased. In this work, the associated momentum transfer is formulated and incorporated into the momentum conservation equation as follows.

D. Variational Formulation

Considering an arbitrary fluid domain (Ω), the rate of the total momentum reads

$$\frac{D}{Dt}\int_\Omega \rho\mathbf{u} d\Omega = \int_\Omega \frac{\partial}{\partial t}(\rho\mathbf{u}) d\Omega + \int_{\partial\Omega}(\rho\mathbf{u})\,\mathbf{u}\cdot\mathbf{n} d(\partial\Omega). \tag{24}$$

Supposing that the boundary of the the arbitrary domain ($\partial\Omega$) partially coincides with the liquid-gas interface (Γ), one has

$$\frac{D}{Dt}\int_\Omega \rho\mathbf{u} d\Omega = \int_\Omega \frac{\partial}{\partial t}(\rho\mathbf{u}) d\Omega + \int_{\partial\Omega\setminus\Gamma}(\rho\mathbf{u})\,\mathbf{u}\cdot\mathbf{n} d(\partial\Omega) + \int_\Gamma (\rho\mathbf{u})\,\mathbf{u}_\Gamma\cdot\mathbf{n} d\Gamma, \tag{25}$$

where $\mathbf{u}_\Gamma = \mathbf{u} + u'_{int}\mathbf{n}$ is the effective (imposed) velocity of the interface, which takes into account both the computed velocity and the contribution of the correction calculated in Eq. (23). This gives

$$\frac{D}{Dt}\int_\Omega \rho\mathbf{u}d\Omega = \int_\Omega \frac{\partial}{\partial t}(\rho\mathbf{u})\,d\Omega + \int_{\partial\Omega}(\rho\mathbf{u})\,\mathbf{u}\cdot\mathbf{n}d(\partial\Omega) + \int_\Gamma (\rho\mathbf{u})\,u'_{int}d\Gamma, \tag{26}$$

or equivalently

$$\frac{D}{Dt}\int_\Omega \rho\mathbf{u}d\Omega = \int_\Omega \left[\frac{\partial}{\partial t}(\rho\mathbf{u}) + \nabla\cdot(\rho\mathbf{u})\right] d\Omega + \int_\Gamma (\rho\mathbf{u})\,u'_{int}d\Gamma. \tag{27}$$

Incorporating the second term on the right-hand-side of Eq. (27), which is associated with the mass conservation correction, and implementing the surface tension condition at the liquid–gas interface (8), the molecular kinetic theory along the contact–line (11), the Navier–slip condition on the solid substrate (14), and Neumann boundary condition (5), the variational form of the momentum conservation equation becomes

$$\begin{aligned}
&\int_\Omega \rho\left(\frac{\partial\mathbf{u}}{\partial t} + \mathbf{u}\cdot\nabla\mathbf{u}\right)\cdot\mathbf{w}d\Omega + \int_\Gamma \rho u'_{int}\mathbf{u}\cdot\mathbf{w}d\Gamma = \int_\Omega \rho\mathbf{b}\cdot\mathbf{w}d\Omega \\
&\quad + \int_\Omega p\nabla\cdot\mathbf{w}d\Omega - \int_\Omega \mu\left(\nabla\mathbf{u} + \nabla\mathbf{u}^T\right):\nabla\mathbf{w}d\Omega \\
&\quad + \int_{\partial\Omega_N}\mathbf{T}_N\cdot\mathbf{w}d(\partial\Omega) - \int_{\partial\Omega_s}\beta\mathbf{u}\cdot\mathbf{w}d(\partial\Omega) - \int_\Gamma \gamma\kappa\mathbf{n}_{int}\cdot\mathbf{w}d\Gamma \\
&\quad + \int_{\partial\Gamma}[(\gamma\mathbf{t}_{int} - \zeta\mathbf{u})\cdot\mathbf{t}_s + \gamma_{gs} - \gamma_{ls}]\,\mathbf{t}_s\cdot\mathbf{w}d(\partial\Gamma).
\end{aligned} \tag{28}$$

In the present work, the test function, $\mathbf{w}$, is chosen from the finite element space. All elements cut by the interface undergo a domain splitting process, which facilitates the accurate calculation of the integrals presented in Eq. (28) and circumvents the need for implementing a regularized delta function. The jump in the pressure field is treated utilizing a pressure–enriched finite element space[46] and the algebraic sub-grid scale technique[59] is used to stabilize the method. For the sake of brevity in this paper, only the new aspects of the present numerical model are discussed, while the detailed description of the enriched finite element framework developed by the authors[46,47] is omitted.

Before moving on and focus on the hysteresis phenomenon, it is worth to analyse the effect of the proposed momentum correction term in a simple test–case, in which an ellipsoidal liquid droplet with its surface being defined as

$$\left(\frac{x-x_c}{a}\right)^2 + \left(\frac{y-y_c}{b}\right)^2 + \left(\frac{x-z_c}{c}\right)^2 = 1,$$

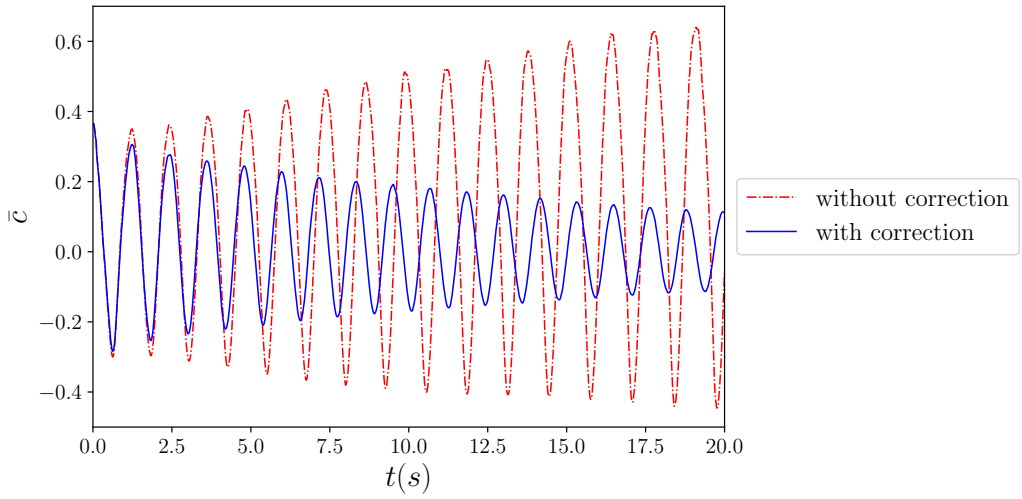

FIG. 3. Time evolution of the amplitude of the oscillating droplet with and without incorporating the momentum correction term.

is confined inside a $1 \times 1 \times 1m^3$ box. Setting $a = b = 0.25m$, $c = 0.4m$, and $x_c = y_c = z_c = 0.5m$, the droplet oscillates until reaching an equilibrium spherical shape with radius $a_{eq} = \sqrt[3]{abc}$. Considering the comparatively large length-scales and consequently, the small curvature, in order to accelerate the droplet deformation, a rather large surface tension of $\gamma = 100N/m$ is used in this test–case along with $\rho_l = 1000kg/m^3$, $\rho_g = 1kg/m^3$, $\mu_l = 1Pa.s$, and $\mu_g = 0.01Pa.s$.

Figure 3 presents the time–evolution of the amplitude of the droplet oscillations along z–axis ($\bar{c}$) that is normalized by a_{eq} for both the corrected and uncorrected formulations. It is evident that without the proposed correction to the momentum equation, the amplitude of the oscillation is growing, contrary to the basic physical expectations. Such behaviour is a cause of numerical instability specially after rather long simulation run–times that obligates significant level–set correction to preserve the mass continuity. It should be noted that in order to highlight the effectiveness of the proposed correction, in the present test–case, the parameters are chosen in a way that the pseudo–velocity associated with the mass conservation correction and consequently, the correction term on the right-hand-side of Eq. (26), be significant. For this test, the Reynolds number is $Re \sim O(10^2)$.

E. Computational Algorithm

In this work, the linearized momentum conservation is implicitly solved together with the mass conservation equation. The computational domain is discretized using linear tetrahedral elements.

Algorithm 1: Time–marching

$n = 1$;

$t = 0$;

while $t <$ *run-time* **do**

- **calculate** nodal contact–angle according to Eq. (21);
- **impose** fixing/unfixing ϕ according to Eq. (15);
- **solve** Eq. (17) for ϕ for the first ***half*** time-step with $\mathbf{u}_n$;
- **reinitialize** ϕ;
- **calculate** curvature as $\kappa = \nabla \cdot (\nabla\phi / \|\nabla\phi\|)$;
- **for** *all elements e* **do**
  - **if** $e \cap \Gamma \neq \varnothing$ **then**
    - **do** element splitting;
    - **impose** pinning condition according to Eq. (16);
    - **calculate** θ according to Eq. (12);
  - **create** elemental system of equations according to Eq. (28);
- **do** assembling the Linear System of Equations (LSE);
- **solve** LSE for $[\mathbf{u}, p]$;
- **solve** Eq. (17) for ϕ for the second ***half*** time-step and the updated $\mathbf{u}$;
- **update** $n = n + 1$;
- **update** $t = n\Delta t$;

TABLE I. Summary of the proposed method.

The convergence of the velocity and pressure fields is obtained by assuring a relative tolerance of 10^{-5}. All the linear systems of equations are solved using the GMRES ($m = 40$) with a convergence tolerance of 10^{-6}. All the implementations are done within KRATOS Multiphysics code[60]. AMGCL library[61] is utilized for solving the linear system of equation. In Table I, the main steps of the proposed numerical method are outlined.

III. RESULTS

In the following, the main test–cases are presented, which are dedicated to the hysteresis phenomenon. Unless otherwise mentioned, the liquid and gas properties correspond to those of water and air, respectively; $\rho_l = 1000kg/m^3$, $\mu_l = 0.001Pa.s$, $\rho_g = 1kg/m^3$, $\mu_g = 0.00001Pa.s$, and $\gamma = 0.072N/m$. Gravity is set to $g = 9.81m/s^2$ in all test–cases.

Computational consistency requires Navier–slip parameter β to be much larger than μ/h_e; in this work, $\beta = 1000Pa.s/m$ passes this criteria for all the meshes. The parameter of the molecular-kinetic model and the microscopic length–scale are set to $\zeta = 0.5Pa.s$ and $l_{micro} = 10^{-9}m$, respectively. These values are within the measured range of the two parameters. Nevertheless, since for the test–cases solved in the present work, an emphasis is given to the pinning (underlying the hysteresis phenomenon) rather than the dynamics of the contact–line, these three parameters have a minor effect on the results. In other words, changing these parameters only affects the dynamics of the droplet spreading on the solid substrate wherever the contact–line is unpinned, while the (final) equilibrium configuration of the droplet is unaffected.

In all cases considered below, the receding and advancing static contact angles of $\theta_R = 115^\circ$ and $\theta_A = 149^\circ$ are considered, respectively. These correspond to experimentally measured values for a water droplet on the outer surface of a typical commercial GDL of a fuel cell[8]. It should be noted that for cases with static contact-angle hysteresis, one cannot provide any equilibrium contact–angle. The contact-angle is subject to variations due to the movement of the contact-line as well as the droplet deformation, which can be active even for a fully pinned droplet. The external forces, e.g. gravity and/or the drag of the air–flow, and droplet inertial oscillations lead to the deformation of partially or fully pinned droplets in the following tests. Not incorporating any prescribed contact–angle, the proposed numerical method is capable of capturing such dynamic behavior. In the present work, all tests are performed in three dimensions and two-dimensional images of the droplets correspond to cross-sections of the three-dimensional domain made at its horizontal plane-of-symmetry if not mentioned otherwise.

A. Water Droplet on Tilted Solid Substrate

First, a test consisting of a water droplet released on top of a (tilted) solid substrate in the presence of gravity is considered. The corresponding schematic is shown in Fig. 4. The ultimate

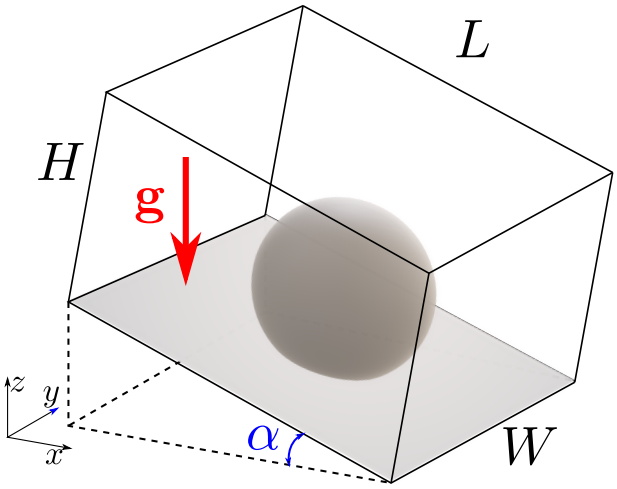

FIG. 4. Schematic of the liquid droplet on a tilted solid substrate.

configuration of the droplet is basically characterized by the hysteresis phenomenon. This test has been widely used as a benchmark for analyzing the hysteresis[8,62–65]. The main aim here is to validate the proposed method and further study the effect of the pinning/unpinning mechanism on the droplet configuration. In this sense, besides the comparison with the experimental data (reported in[8]), this section also includes the results of the (same) test–cases re–simulated without the explicit imposition of the pinning condition (15).

In this section, the volume of the droplet is set to $10\mu L$ and the time–step is $\Delta t = 10^{-5}s$ for all cases. Figure 5 shows the initial (spherical-cap) configuration of the water droplet. For this configuration, one obtains the volume of the droplet as

$$\mathscr{V}_{liq} = \int_0^{\theta_0} \pi R_0^3 \sin^3(\theta) d\theta = \frac{\pi R_0^3}{3}\left[2 - 3\cos(\theta_0) + \cos^3(\theta_0)\right].$$

Once the liquid volume is set, the initial radius (R_0) and vertical offset $Z_0 = R_0 \sin(\theta_0 - 90^\circ)$ are calculated. It is important to note that the numerical results with $\theta_0 < 180^\circ$ can be compared to the experimental results with $\theta_0 = 180^\circ$ only if $\theta_0 > \theta_{avd}$. For the present test–case, the initial contact–angle is set to $\theta_0 = 155^\circ$.

It must be noted that an important physical phenomenon here is the occurrence of oscillations, which are rooted in the concurrent effect of inertia and surface tension[8,66,67]. In order to prevent strong droplet oscillations in this section, first, the gravity is linearly increased from zero to $g = 9.81 m/s^2$ with a slope of g/τ_r while the tilting angle is kept zero. Then, the tilting angle is increased from zero to α following a linear trend with the slope of $\pi/(18\tau_r)$. In this test, the relaxation time is set to $\tau_r = 0.01s$. In the actual experiments, similar precautions are followed by

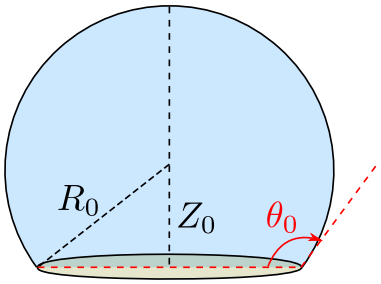

FIG. 5. Schematic of the initial configuration of the liquid droplet.

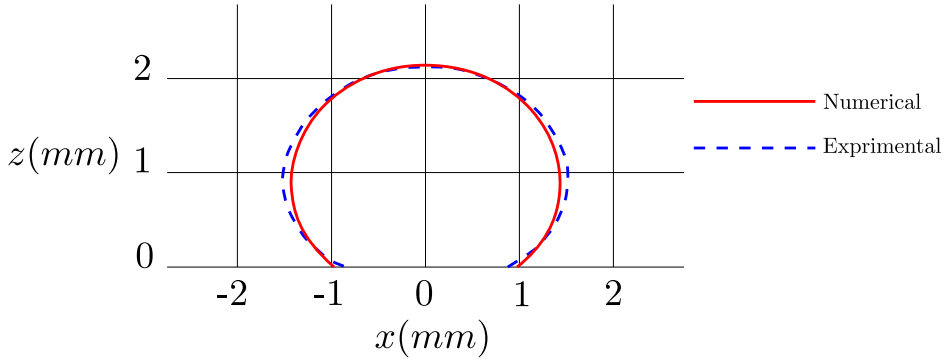

FIG. 6. Comparison of the numerical result with the experimental result reported in[8] for zero tilting angle.

slowly releasing the droplet from the injection tip and gradually inclining the solid plane.

In this section, the computational mesh corresponding to $R_0/h \approx 11.0$ is composed of $\sim 350K$ elements and $\sim 75K$ nodes leading to $\sim 300K$ degrees–of–freedom. We shall consider this mesh as "standard" and it will be used by default in the simulations. In case of using a different mesh resolution, it will be explicitly specified. Using this setup, for each test–case, reaching the physical time of $t = 0.1s$ (or equivalently 10^4 time–steps for the present case) in the simulation requires almost 80 hours of run–time on 4 cores of a PC equipped with an Intel® Core™ i7-4770 processor. In this sense, the prohibitive computational cost associated with very long simulation times, impedes the use of an extremely large relaxation time.

Figure 6 illustrates the numerically obtained interface of the droplet on the xz–plane for the zero–tilting ($\alpha = 0$) case in comparison with the experimental result reported in[8]. The results are in a good agreement. The difference between the simulated footprint radius and its experimental value is $\sim 10\%$.

In order to check the effect of mesh resolution, the same test was also simulated on a coarser and a finer mesh with $R_0/h \approx 8.3$ and $R_0/h \approx 13.8$, respectively. In order to verify the mesh–

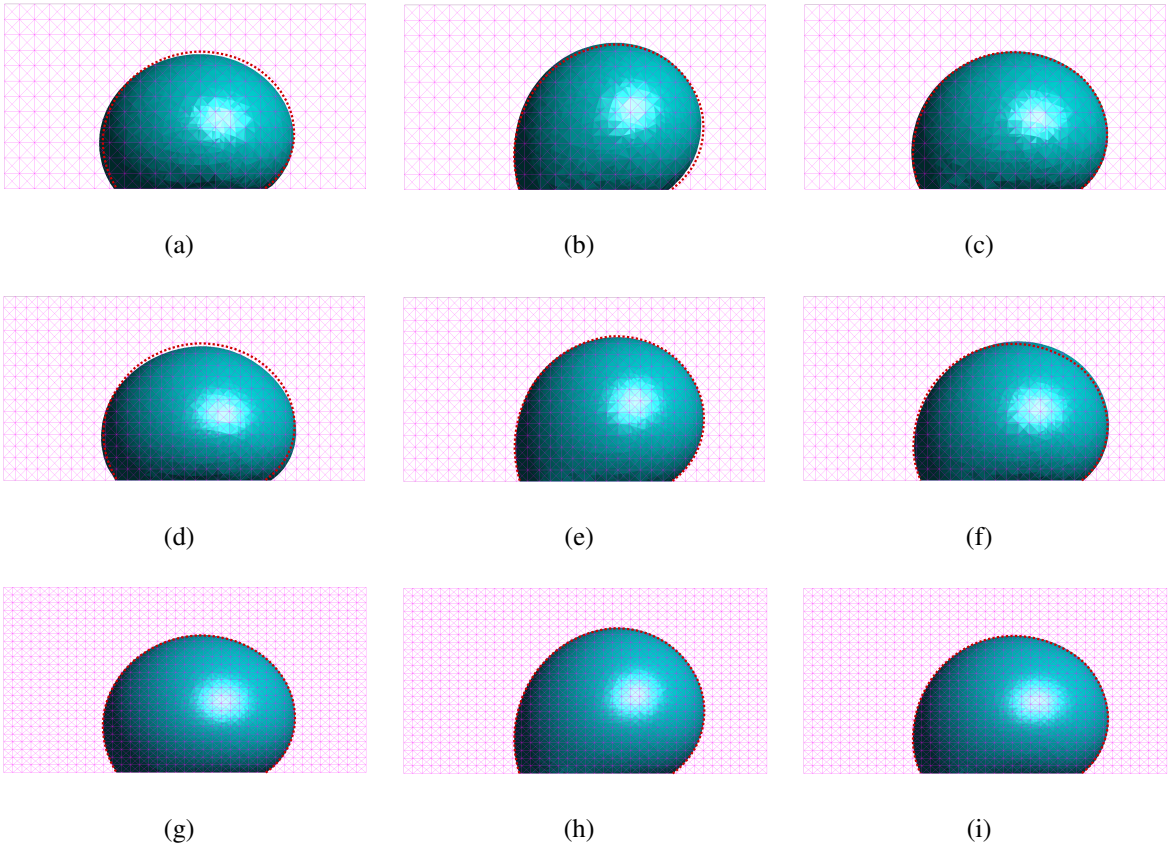

FIG. 7. Comparison of the configuration of the droplet obtained at (a,d,g) $t = 0.035s$, (b,e,h) $t = 0.045s$, and (c,f,i) $t = 0.055s$. In the first row, (a,b,c) the results are shown for the coarsest mesh size, $R_0/h \approx 8.3$. The second and third rows correspond to the mesh sizes of $R_0/h \approx 11.0$ and 13.8, respectively. The dotted–lines are fitted to the droplet configurations obtained for the finest mesh and replicated on the other figures for the sake of comparison.

independence for a more rigorous test–case, here, the tilting angle is set to $\alpha = 30^\circ$. Therefore, in this test, once the magnitude of the gravity reaches $9.81 m/s^2$, the tilting angle is dynamically increasing from zero up to 30 degrees. The resulting droplet configurations are presented in Fig. 7 at three different instances in time. In this figure, the generated computational meshes are also illustrated. It is important to mention that in this test, droplet is continuously deforming under the effects of a dynamic gravitational force, surface tension, and the inertia. The excellent match between the results obtained for different mesh resolutions is evident in Fig. 7. Thus, the rest of the simulations are all performed with $R_0/h \approx 11.0$.

Upon increasing the tilting angle, θ_a increases and θ_r decreases until the pinning threshold (determined by θ_A and θ_R) is surpassed and consequently, the droplet is detached. In Fig. 8, the

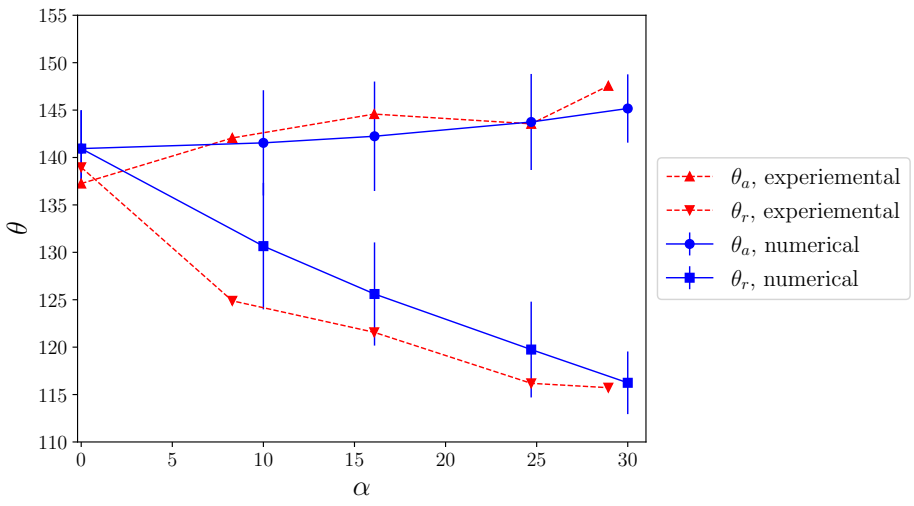

FIG. 8. Comparison of the numerical results with the experimental results reported in[8] for different tilting angles.

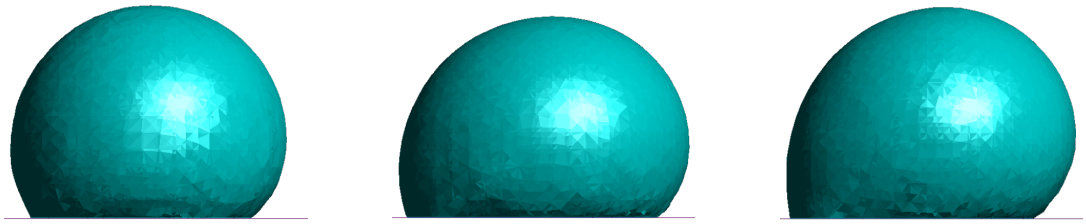

(a) (b) (c)

FIG. 9. Droplet configuration obtained with pinning mechanism for different tilting angles, (a) $\alpha = 10^\circ$, (b) $\alpha = 30^\circ$, and (c) $\alpha = 50^\circ$.

instantaneous contact–angle hysteresis (in terms of θ_a and θ_r) of a pinned droplet attached to a tilted solid substrate is compared with the experimental data[8]. The error bars in Fig. 8 show the standard deviation of the result associated with the averaging of the advancing and the receding contact–angles. The agreement between the numerical and experimental results is observed in Fig. 8. The side view of the droplet and the configuration of its contact–line are presented in Figs. 9 and 10, respectively. These figures also include the result for $\alpha = 50^\circ$, for which the droplet detachment occurred. The presented results correspond to the instances when the droplet has nearly reached a terminal shape. Nonetheless, droplet oscillations are present, leading to slight deformations in–time.

Next, it is worth to investigate the same test–case without explicit imposition of the contact–

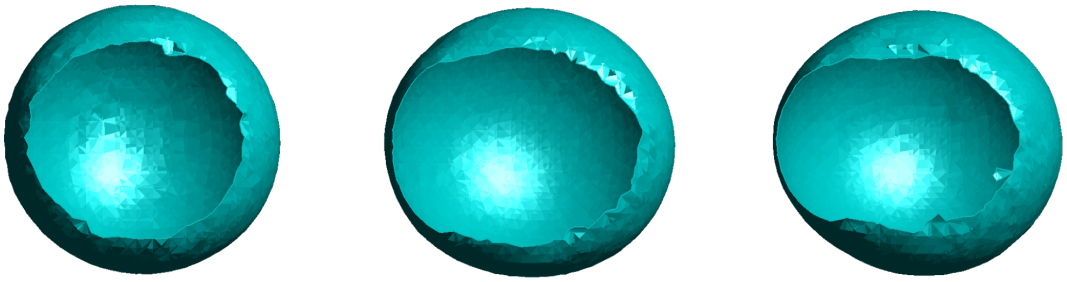

(a) (b) (c)

FIG. 10. The configuration of the contact–line obtained with pinning mechanism for different tilting angles, (a) $\alpha = 10^\circ$, (b) $\alpha = 30^\circ$, and (c) $\alpha = 50^\circ$.

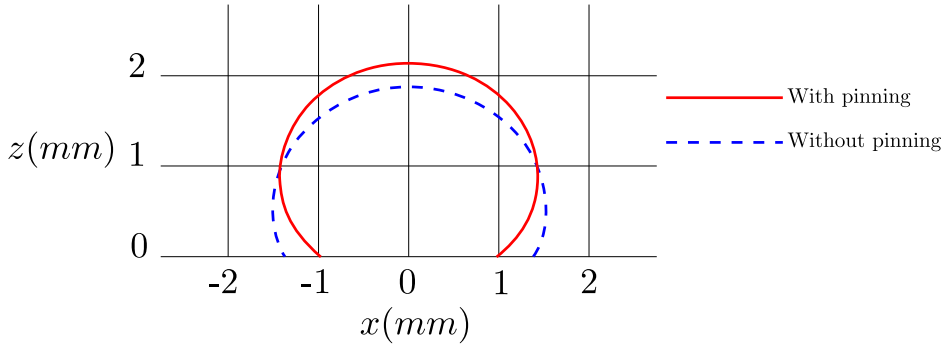

FIG. 11. Comparison of the numerical results with and without imposing the pinning mechanism.

line pinning/unpinning threshold. The present methodology allows for performing such simulations directly by setting $\theta_A = \theta_R = \theta_{eq}$. In the presence of static contact–angle hysteresis, the corresponding droplet adhesion (pinning) force is proportional to $\gamma|\cos(\theta_R) - \cos(\theta_A)|$[45,68]. Consequently, and taking into account that in the absence of the static contact–angle hysteresis, the net surface force acting on the contact–line is measured as $\gamma\cos(\theta_{eq})$, the corresponding equilibrium contact–angle can be estimated as

$$\theta_{eq} = \cos^{-1}\left(\frac{1}{2}\left[\cos(115^\circ) + \cos(149^\circ)\right]\right) \approx 129.8^\circ.$$

As expected and shown in Fig. 11, without a pinning mechanism, the droplet is spread more. Without a pinning mechanism, the instantaneous contact–angle hysteresis, $\Delta\theta = \theta_a - \theta_r$, is also significantly smaller as seen in Fig. 12 compared to Fig. 9. In the absence of a pinning mechanism, the frictional effect on the solid substrate is responsible for the manifestation of the (dynamic) contact–line hysteresis. The corresponding configurations of the contact–line are also presented

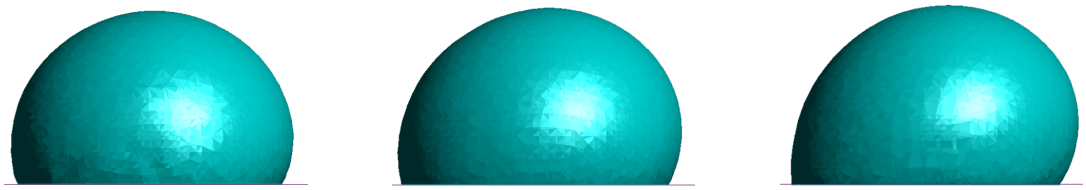

(a) (b) (c)

FIG. 12. The configuration of the contact–line obtained without pinning mechanism for different tilting angles, (a) $\alpha = 10^\circ$, (b) $\alpha = 30^\circ$, and (c) $\alpha = 50^\circ$.

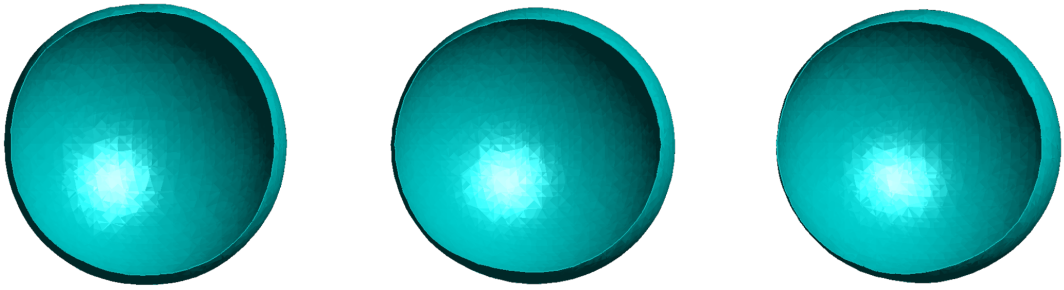

(a) (b) (c)

FIG. 13. The configuration of the contact–line obtained without pinning mechanism for different tilting angles, (a) $\alpha = 10^\circ$, (b) $\alpha = 30^\circ$, and (c) $\alpha = 50^\circ$.

in Fig. 13.

B. Water Droplet Exposed to the Airflow in a Gas Channel

In the following tests, the computational domain is similar to the one schematically shown in Fig. 4, however, without tilting ($\alpha = 0$). The domain sizes are $L = 800\mu m$, $W = 300\mu m$, and $H = 200\mu m$. Here, a water droplet of $R_0 = 107\mu m$ is positioned on the solid substrate with the initial contact–angle of $\theta_0 = 90^\circ$ and is subject to an air–flow. The inlet boundary condition is defined by applying fixed prescribed velocity of

$$u = \begin{cases} \frac{u_0}{2}\left[1 - \cos\left(\frac{\pi}{0.001}t\right)\right] & \text{if } t \leq 0.001s \\ u_0 & \text{if } t > 0.001s \end{cases}$$

in x–direction, and at the outlet, a constant (zero) pressure boundary condition is imposed. The rather large relaxation time of $0.001s$ provides the droplet enough time to obtain contact–angles

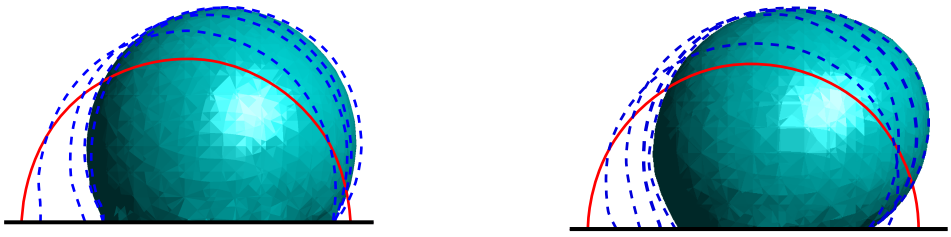

(a) (b)

FIG. 14. Evolution of the interface of the droplet subject to air–flow with (a) $u_0 = 2m/s$ and (b) $u_0 = 6m/s$. The outline of the evolving interface is shown with dashed–line, while the solid–line corresponds to the initial configuration of the droplet.

significantly larger than 90° according to the hydrophobicity of the substrate, before the imposition of the maximum velocity. Moreover, the droplet is initially $1.5H$ away from the inlet in order to minimize the effect of spatially uniform velocity set at the boundary of the domain. Here, the time–step is set to $\Delta t = 10^{-6}s$ and the computational domain is discretized by $\sim 250K$ elements.

Figure 14 shows the evolution of the droplet until reaching its terminal configuration for cases with $u_0 = 2m/s$ and $u_0 = 6m/s$. The corresponding Reynolds numbers are $Re = 55$ and 166, based on the hydraulic diameter of the channel and air properties. It is observed that by increasing the air–flow velocity, the contact–line sweeps a larger distance both at the receding and advancing fronts of the droplet. As expected, the larger drag force also leads to a significant increase in θ_a. This is further presented in Table II, which provides the contact–angle hysteresis, along with θ_a and θ_r, for the equilibrium configuration of the droplet. Besides the increase in θ_a, by increasing

TABLE II. Contact–angle hysteresis obtained for different u_0.

u_0	$\theta_a(^\circ)$	$\theta_r(^\circ)$	$\Delta\theta(^\circ)$
$2m/s$	135.6 ± 1.5	124.4 ± 1.5	11.2 ± 2.1
$4m/s$	139.3 ± 2.2	128.0 ± 1.1	11.3 ± 2.5
$5m/s$	140.8 ± 1.6	128.5 ± 2.2	12.3 ± 2.8
$6m/s$	150.0 ± 1.8	131.3 ± 1.3	18.7 ± 2.2

the velocity of the air–flow, a slight increase in θ_r is also observed. The rate of the change in θ_a dramatically increases by approaching the threshold of droplet detachment, which is $u_0 = 6m/s$ in this case.

It is important to mention that hysteresis must be observed as a three–dimensional phenomenon and droplet detachment cannot be judged by taking into account only the contact–angles at the advancing and receding fronts. This indicates that using 2D approximations may lead to erroneous conclusions regarding the prediction of droplet detachment, since the lateral parts of the droplet might well be pinned, while the angle in the vicinity of triple–points (2D counterpart of the contact line) on the axis–of–symmetry exceed the threshold. This can clearly be seen for example in the above test–case with $u_0 = 6m/s$, where although the advancing contact–angle has already reached θ_A, still the major part of the contact–line is pinned and consequently the droplet retains its location.

Velocity vectors on a vertical and a horizontal cross–section are shown in Fig. 15 for $u_0 = 6m/s$. The onset of a wake adjacent to the droplet in the downstream is detectable in Fig. 15(a). By further increasing the inlet velocity, such complex features of the air–flow become more significant and therefore, in order to adequately capture the physical phenomena, a more refined computational mesh and/or special numerical treatments that are generally categorized within the context of turbulent flow modeling are required.

IV. CONCLUSION

A level–set/enriched finite element method that have been developed by the authors, was further advanced in this work by including the pinning mechanism along with other "ingredients" necessary for successful modeling of the hysteresis phenomenon. A modification to the momentum equation was proposed to incorporate the effect of the mass-conservation correction and its performance was analyzed in the simple test of a freely oscillating droplet. The present numerical model was validated for a benchmark involving a water droplet placed on a tilted plane. It was also shown that if the pinning is absent, a dynamic contact–angle hysteresis is still observable due to the frictional forces acting at the surface of the solid substrate. This however, is much smaller than the experimentally detected static contact–angle hysteresis occurring in the presence of pinning.

The numerical model was also employed to simulate a water droplet confined in a channel and exposed to an air–flow with Reynolds numbers ranging from $Re \sim 50$ to 150. It is necessary to mention that for these tests, it was hardly possible to capture all the features of the air–flow on a rather coarse computational mesh that was employed. These features become more important as the Reynolds number increases. For capturing such effects, a significantly finer mesh resolution

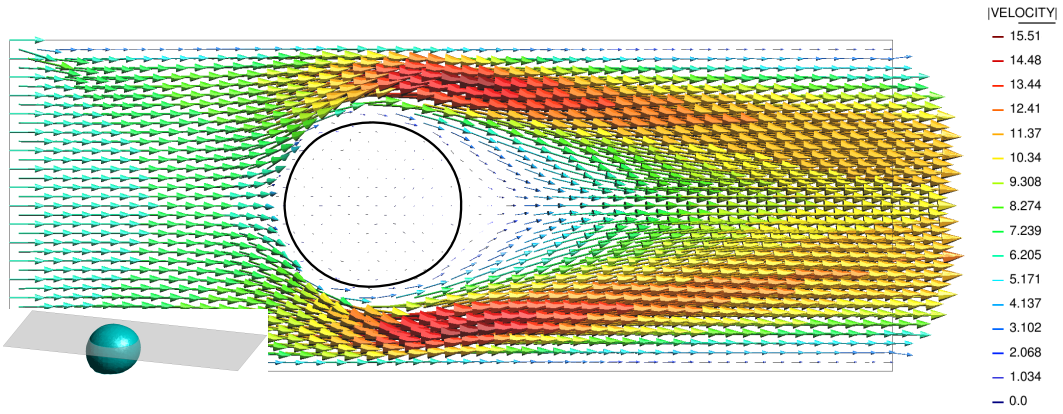

(a)

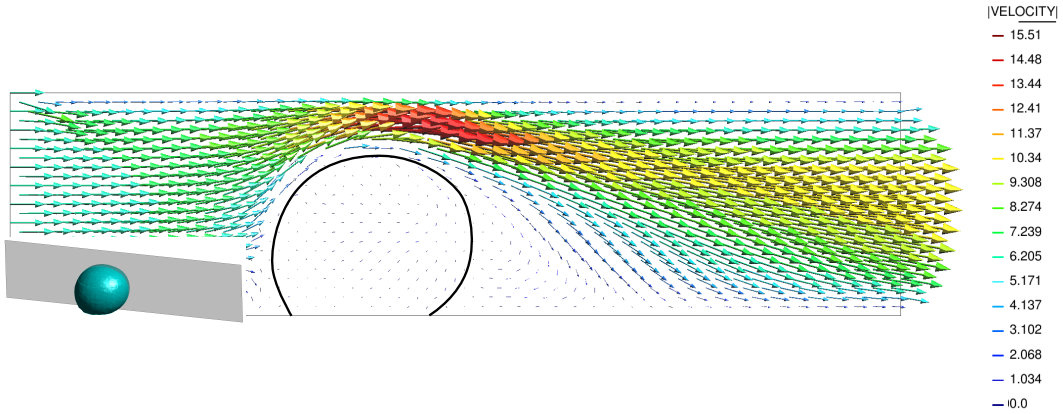

(b)

FIG. 15. Velocity vectors around the droplet subject to air–flow with $u_0 = 6m/s$. Cross–sectional views perpendicular to (a) y–axis and (b) z–axis.

and consequently, prohibitively higher computational costs are needed for the accurate simulation of the time–evolution of the droplet configuration at larger Reynolds numbers.

Overall, the simulations performed indicate that the proposed approach (three-dimensional enriched finite element/level set method) is capable of providing important insights regarding behavior of droplets contacting solid substrates accounting for dynamic contact line with hysteresis. Moreover, reproducing the interfacial discontinuity in a sharp way allows employing relatively coarse meshes that facilitate performing 3D simulations in reasonable execution time.

ACKNOWLEDGMENT

This work was performed within the framework of AMADEUS project ("Advanced Multi-scAle moDEling of coupled mass transport for improving water management in fUel cellS", reference number PGC2018-101655-B-I00) supported by the *Ministerio de Ciencia, Innovacion e Universidades* of Spain. The authors acknowledge financial support of the mentioned Ministry via the “Severo Ochoa Programme" for Centres of Excellence in R&D (referece: CEX2018-000797-S) given to the International Centre for Numerical Methods in Engineering (CIMNE). The authors also acknowledge PRACE for awarding us access to MareNostrum hosted by Barcelona Supercomputing Center, Spain (project reference: 2010PA5560).

CONFLICT OF INTEREST

The authors declare that they have no conflict of interest.

DATA AVAILABILITY STATEMENT

The data that support the findings of this study are available from the corresponding author upon reasonable request.

REFERENCES

[1]F. Barbir, *PEM Fuel Cells: Theory and Practice* (Academic Press, 2012) google-Books-ID: elO7n4Z6uLoC.

[2]M. Contestabile, “Analysis of the market for diesel PEM fuel cell auxiliary power units onboard long-haul trucks and of its implications for the large-scale adoption of PEM FCs,” Energy Policy The socio-economic transition towards a hydrogen economy - findings from European research, with regular papers, **38**, 5320–5334 (2010).

[3]T. Fletcher, R. Thring, and M. Watkinson, “An Energy Management Strategy to concurrently optimise fuel consumption & PEM fuel cell lifetime in a hybrid vehicle,” International Journal of Hydrogen Energy **41**, 21503–21515 (2016).

[4]P. C. Okonkwo and C. Otor, "A review of gas diffusion layer properties and water management in proton exchange membrane fuel cell system," International Journal of Energy Research **45**, 3780–3800 (2021), _eprint: https://onlinelibrary.wiley.com/doi/pdf/10.1002/er.6227.

[5]M. Grimm, M. Hellmann, H. Kemmer, and S. Kabelac, "Water Management of PEM Fuel Cell Systems Based on the Humidity Distribution in the Anode Gas Channels," Fuel Cells **20**, 477–486 (2020), _eprint: https://onlinelibrary.wiley.com/doi/pdf/10.1002/fuce.202000070.

[6]T. C. Wu and N. Djilali, "Experimental investigation of water droplet emergence in a model polymer electrolyte membrane fuel cell microchannel," Journal of Power Sources **208**, 248–256 (2012).

[7]X. Zhu, P. C. Sui, and N. Djilali, "Three-dimensional numerical simulations of water droplet dynamics in a PEMFC gas channel," Journal of Power Sources SPECIAL SECTION Selected papers from the 1st POLISH FORUM ON FUEL CELLS AND HYDROGEN, **181**, 101–115 (2008).

[8]A. Jarauta, P. Ryzhakov, M. Secanell, P. R. Waghmare, and J. Pons-Prats, "Numerical study of droplet dynamics in a polymer electrolyte fuel cell gas channel using an embedded Eulerian-Lagrangian approach," Journal of Power Sources **323**, 201–212 (2016).

[9]A. Theodorakakos, T. Ous, M. Gavaises, J. M. Nouri, N. Nikolopoulos, and H. Yanagihara, "Dynamics of water droplets detached from porous surfaces of relevance to PEM fuel cells," Journal of Colloid and Interface Science **300**, 673–687 (2006).

[10]M. Andersson, V. Vukčević, S. Zhang, Y. Qi, H. Jasak, S. B. Beale, and W. Lehnert, "Modeling of droplet detachment using dynamic contact angles in polymer electrolyte fuel cell gas channels," International Journal of Hydrogen Energy **44**, 11088–11096 (2019).

[11]X. Zhang and Y. Qin, "Contact angle hysteresis of a water droplet on a hydrophobic fuel cell surface," Journal of Colloid and Interface Science **545**, 231–241 (2019).

[12]E. Gauthier, T. Hellstern, I. G. Kevrekidis, and J. Benziger, "Drop Detachment and Motion on Fuel Cell Electrode Materials," ACS Applied Materials & Interfaces **4**, 761–771 (2012), publisher: American Chemical Society.

[13]D. Seveno, A. Vaillant, R. Rioboo, H. Adao, J. Conti, and J. De Coninck, "Dynamics of wetting revisited," Langmuir **25**, 13034–13044 (2009), publisher: ACS Publications.

[14]T. Young, "III. An essay on the cohesion of fluids," Philosophical Transactions of the Royal Society of London **95**, 65–87 (1805), publisher: Royal Society.

[15]A. Hamraoui, K. Thuresson, T. Nylander, and V. Yaminsky, "Can a Dynamic Contact Angle Be Understood in Terms of a Friction Coefficient?" Journal of Colloid and Interface Science **226**, 199–204 (2000).

[16]W. Qi and P. B. Weisensee, "Dynamic wetting and heat transfer during droplet impact on bi-phobic wettability-patterned surfaces," Physics of Fluids **32**, 067110 (2020), publisher: American Institute of Physics.

[17]M. Kumar, R. Bhardwaj, and K. C. Sahu, "Coalescence dynamics of a droplet on a sessile droplet," Physics of Fluids **32**, 012104 (2020), publisher: American Institute of Physics.

[18]R. Bhardwaj and A. Agrawal, "Likelihood of survival of coronavirus in a respiratory droplet deposited on a solid surface," Physics of Fluids **32**, 061704 (2020), publisher: American Institute of Physics.

[19]T. D. Blake and J. M. Haynes, "Kinetics of liquidliquid displacement," Journal of Colloid and Interface Science **30**, 421–423 (1969).

[20]L. Zhao and J. Cheng, "Analyzing the Molecular Kinetics of Water Spreading on Hydrophobic Surfaces via Molecular Dynamics Simulation," Scientific Reports **7**, 10880 (2017).

[21]R. G. Cox, "The dynamics of the spreading of liquids on a solid surface. Part 1. Viscous flow," Journal of Fluid Mechanics **168**, 169 (1986).

[22]J.-H. Kim, H. P. Kavehpour, and J. P. Rothstein, "Dynamic contact angle measurements on superhydrophobic surfaces," Physics of Fluids **27**, 032107 (2015), publisher: American Institute of Physics.

[23]J.-C. Fernández-Toledano, T. D. Blake, and J. De Coninck, "Taking a closer look: A molecular-dynamics investigation of microscopic and apparent dynamic contact angles," Journal of Colloid and Interface Science **587**, 311–323 (2021).

[24]A. M. Karim, K. Fujii, and H. P. Kavehpour, "Contact line dynamics of gravity driven spreading of liquids," Fluid Dynamics Research **53**, 035503 (2021), publisher: IOP Publishing.

[25]P. Petrov and I. Petrov, "A combined molecular-hydrodynamic approach to wetting kinetics," Langmuir **8**, 1762–1767 (1992), publisher: ACS Publications.

[26]H. B. Eral, D. J. C. M. 't Mannetje, and J. M. Oh, "Contact angle hysteresis: a review of fundamentals and applications," Colloid and Polymer Science **291**, 247–260 (2013).

[27]Q. Liu, J. Yu, and H. Wang, "The role of the substrate roughness in contact angle hysteresis and dynamic deviation," International Journal of Heat and Mass Transfer **148**, 118985 (2020).

[28]P. G. de Gennes, "Wetting: statics and dynamics," Reviews of Modern Physics **57**, 827–863 (1985).

[29]L. Gao and T. J. McCarthy, "Contact Angle Hysteresis Explained," Langmuir **22**, 6234–6237 (2006), publisher: American Chemical Society.

[30]C. W. Extrand and Y. Kumagai, "Liquid Drops on an Inclined Plane: The Relation between Contact Angles, Drop Shape, and Retentive Force," Journal of Colloid and Interface Science **170**, 515–521 (1995).

[31]S. Brandon, A. Wachs, and A. Marmur, "Simulated Contact Angle Hysteresis of a Three-Dimensional Drop on a Chemically Heterogeneous Surface: A Numerical Example," Journal of Colloid and Interface Science **191**, 110–116 (1997).

[32]M. Hatipogullari, C. Wylock, M. Pradas, S. Kalliadasis, and P. Colinet, "Contact angle hysteresis in a microchannel: Statics," Physical Review Fluids **4**, 044008 (2019), publisher: American Physical Society.

[33]D. Quéré, "Wetting and Roughness," Annual Review of Materials Research **38**, 71–99 (2008), _eprint: https://doi.org/10.1146/annurev.matsci.38.060407.132434.

[34]S. Qiao, Q. Li, and X.-Q. Feng, "Sliding friction and contact angle hysteresis of droplets on microhole-structured surfaces," The European Physical Journal E **41**, 25 (2018).

[35]Y. Di, J. Qiu, G. Wang, H. Wang, L. Lan, and B. Zheng, "Exploring Contact Angle Hysteresis Behavior of Droplets on the Surface Microstructure," Langmuir **37**, 7078–7086 (2021), publisher: American Chemical Society.

[36]H.-Y. Kim, S. Jeon, M. Song, and K. Kim, "Numerical simulations of water droplet dynamics in hydrogen fuel cell gas channel," Journal of Power Sources **246**, 679–695 (2014).

[37]J. Yang, X. Ma, L. Fei, X. Zhang, K. H. Luo, and S. Shuai, "Effects of hysteresis window on contact angle hysteresis behaviour at large Bond number," Journal of Colloid and Interface Science **566**, 327–337 (2020).

[38]P. Yue, "Thermodynamically consistent phase-field modelling of contact angle hysteresis," Journal of Fluid Mechanics **899** (2020), 10.1017/jfm.2020.465, publisher: Cambridge University Press.

[39]C. Fang, C. Hidrovo, F.-m. Wang, J. Eaton, and K. Goodson, "3-D numerical simulation of contact angle hysteresis for microscale two phase flow," International Journal of Multiphase Flow **34**, 690–705 (2008), publisher: Elsevier.

[40]J. Zhang and P. Yue, "A level-set method for moving contact lines with contact angle hysteresis," Journal of Computational Physics , 109636 (2020), publisher: Elsevier.

[41]Y. F. Yap, J. C. Chai, T. N. Wong, K. C. Toh, and H. Y. Zhang, "A Global Mass Correction Scheme for the Level-Set Method," Numerical Heat Transfer, Part B: Fundamentals **50**, 455–472 (2006), publisher: Taylor & Francis _eprint: https://doi.org/10.1080/10407790600646958.

[42]Z. Solomenko, P. D. M. Spelt, L. Ó Náraigh, and P. Alix, "Mass conservation and reduction of parasitic interfacial waves in level-set methods for the numerical simulation of two-phase flows: A comparative study," International Journal of Multiphase Flow **95**, 235–256 (2017).

[43]Z. Ge, J.-C. Loiseau, O. Tammisola, and L. Brandt, "An efficient mass-preserving interface-correction level set/ghost fluid method for droplet suspensions under depletion forces," Journal of Computational Physics **353**, 435–459 (2018).

[44]E. Mahrous, A. Jarauta, T. Chan, P. Ryzhakov, A. Z. Weber, R. V. Roy, and M. Secanell, "A particle finite element-based model for droplet spreading analysis," Physics of Fluids **32**, 042106 (2020), publisher: AIP Publishing LLC.

[45]E. Mahrous, R. V. Roy, A. Jarauta, and M. Secanell, "A two-dimensional numerical model for the sliding motion of liquid drops by the particle finite element method," Physics of Fluids **33**, 032117 (2021), publisher: American Institute of Physics.

[46]M. R. Hashemi, P. B. Ryzhakov, and R. Rossi, "An enriched finite element/level-set method for simulating two-phase incompressible fluid flows with surface tension," Computer Methods in Applied Mechanics and Engineering **370**, 113277 (2020).

[47]M. R. Hashemi, P. B. Ryzhakov, and R. Rossi, "Three dimensional modeling of liquid droplet spreading on solid surface: An enriched finite element/level-set approach," Journal of Computational Physics **442**, 110480 (2021).

[48]E. B. Dussan, "On the Spreading of Liquids on Solid Surfaces: Static and Dynamic Contact Lines," Annual Review of Fluid Mechanics **11**, 371–400 (1979).

[49]D. Seveno, T. D. Blake, and J. De Coninck, "Young's Equation at the Nanoscale," Physical Review Letters **111**, 096101 (2013), publisher: American Physical Society.

[50]F. Brochard-Wyart and P. G. de Gennes, "Dynamics of partial wetting," Advances in Colloid and Interface Science **39**, 1–11 (1992).

[51]L. M. Pismen, "Some singular errors near the contact line singularity, and ways to resolve both," The European Physical Journal Special Topics **197**, 33 (2011).

[52]W. Ren and W. E, "Boundary conditions for the moving contact line problem," Physics of fluids **19**, 022101 (2007), publisher: American Institute of Physics.

[53]V. Starov, "Static contact angle hysteresis on smooth, homogeneous solid substrates," Colloid and Polymer Science **291**, 261–270 (2013).

[54]M. Sussman, P. Smereka, and S. Osher, "A level set approach for computing solutions to incompressible two-phase flow," Journal of Computational physics **114**, 146–159 (1994), publisher: Elsevier.

[55]R. N. Elias, M. A. Martins, and A. L. Coutinho, "Simple finite element-based computation of distance functions in unstructured grids," International journal for numerical methods in engineering **72**, 1095–1110 (2007), publisher: Wiley Online Library.

[56]R. Codina, "A discontinuity-capturing crosswind-dissipation for the finite element solution of the convection-diffusion equation," Computer Methods in Applied Mechanics and Engineering **110**, 325–342 (1993).

[57]M. Sussman and E. G. Puckett, "A Coupled Level Set and Volume-of-Fluid Method for Computing 3D and Axisymmetric Incompressible Two-Phase Flows," Journal of Computational Physics **162**, 301–337 (2000).

[58]R. Nourgaliev, S. Wiri, N. Dinh, and T. Theofanous, "Adaptive Strategies for Mass Conservation in Level Set Treatment," in *17th AIAA Computational Fluid Dynamics Conference* (American Institute of Aeronautics and Astronautics) _eprint: https://arc.aiaa.org/doi/pdf/10.2514/6.2005-5348.

[59]R. Codina, S. Badia, J. Baiges, and J. Principe, "Variational multiscale methods in computational fluid dynamics," in *Encyclopedia of Computational Mechanics Second Edition* (Wiley Online Library, 2018) pp. 1–28.

[60]P. Dadvand, R. Rossi, and E. Oñate, "An Object-oriented Environment for Developing Finite Element Codes for Multi-disciplinary Applications," Archives of Computational Methods in Engineering **17**, 253–297 (2010).

[61]D. Demidov, "AMGCL —A C++ library for efficient solution of large sparse linear systems," Software Impacts **6**, 100037 (2020).

[62]D. Quéré, M.-J. Azzopardi, and L. Delattre, "Drops at Rest on a Tilted Plane," Langmuir **14**, 2213–2216 (1998), publisher: American Chemical Society.

[63]N. L. Grand, A. Daerr, and L. Limat, "Shape and motion of drops sliding down an inclined plane," Journal of Fluid Mechanics **541**, 293–315 (2005), publisher: Cambridge University

Press.

[64]J. Hyväluoma, A. Koponen, P. Raiskinmäki, and J. Timonen, "Droplets on inclined rough surfaces," The European Physical Journal E **23**, 289–293 (2007).

[65]Y. H. Yeong, A. Milionis, E. Loth, and I. S. Bayer, "Microscopic Receding Contact Line Dynamics on Pillar and Irregular Superhydrophobic Surfaces," Scientific Reports **5**, 8384 (2015), bandiera_abtest: a Cc_license_type: cc_by Cg_type: Nature Research Journals Number: 1 Primary_atype: Research Publisher: Nature Publishing Group Subject_term: Nanoparticles;Surface assembly Subject_term_id: nanoparticles;surface-assembly.

[66]A. J. B. Milne and A. Amirfazli, "Drop Shedding by Shear Flow for Hydrophilic to Superhydrophobic Surfaces," Langmuir **25**, 14155–14164 (2009), publisher: American Chemical Society.

[67]S. Burgmann, M. Dues, B. Barwari, J. Steinbock, L. Büttner, J. Czarske, and U. Janoske, "Flow measurements in the wake of an adhering and oscillating droplet using laser-Doppler velocity profile sensor," Experiments in Fluids **62**, 47 (2021).

[68]G. Yang, X. Chu, V. Vaikuntanathan, S. Wang, J. Wu, B. Weigand, and A. Terzis, "Droplet mobilization at the walls of a microfluidic channel," Physics of Fluids **32**, 012004 (2020), publisher: American Institute of Physics.